LASER & PHOTONICS REVIEWS
www.lpr-journal.org

Anisotropic and Temperature-Tunable Second-Harmonic Vortex Generation in Ferroelectric $NbOCl_2$ Holograms

Jayanta Deka, Xiaodong Yang, and Jie Gao**

Optical vortex beams with helical phase fronts have immense potential to enhance data capacity due to the unbounded values of orbital angular momentum. Chip-scale platforms for producing vortex beams are of paramount importance for a variety of applications. On the other hand, 2D materials with unique optical properties are essential for developing multifunctional ultrathin photonic devices. Here, anisotropic and temperature-tunable second-harmonic vortex beam generation is demonstrated with ultrathin ferroelectric niobium oxide dichloride ($NbOCl_2$) fork holograms. The polarization-resolved Raman measurements are performed on the $NbOCl_2$ crystal to understand the anisotropic behavior of the Raman modes. It is demonstrated that the anisotropic and temperature-tunable second-harmonic vortex beams can be generated regardless of the relative orientation of the fork gratings with respect to the crystallographic orientation of the $NbOCl_2$ flakes. Furthermore, the Curie temperature of the ferroelectric $NbOCl_2$ crystal is determined according to the measured temperature-dependent second-harmonic generation intensities. The results presented here create new opportunities for the development of advanced polarization-sensitive and temperature-switchable nonlinear photonic devices used for future applications in integrated photonic devices, quantum optical chips, and optical communication.

1. Introduction

Optical vortex beams possess helical phase fronts with the phase term of $e^{il\phi}$ where l represents the topological charge (TC) of the vortex. The orbital angular momentum (OAM) carried by an optical vortex beam has an unbounded value of $l\hbar$ per photon, which enables multiplexing of data streams in optical communication and information processing, offering great potential to enhance data capacity.[1,2] Along with this, optical vortex beams have found applications in a wide range of fields, including optical trapping,[3] optical tweezers,[4] quantum technologies,[5] and optical metrology.[6] The traditional approaches of generating optical vortex beams using spatial light modulators and spiral phase plates are not compatible with photonic integration due to the large size of the components. The development of chip-scale platforms for producing optical vortex beams is of paramount importance for a variety of applications. Plasmonic metasurfaces have been utilized to generate optical vortex beams,[7–9] but they often suffer from large optical absorption and low nonlinear conversion efficiency.

Different types of 2D materials have been attracting significant research interest due to their versatile optical properties for building chip-scale multifunctional ultrathin optical devices. Strong and tailorable nonlinear optical responses of various 2D materials have been explored, which have great potential for realizing compact nonlinear photonic devices.[10–12] The reduced dimensionality of 2D materials also makes them an excellent platform to build nonlinear photonic devices without phase-matching constraints. Recently, niobium oxide dihalides ($NbOX_2$) (X = Cl, Br, I), as a new class of 2D ferroelectric materials, have been studied for applications in nonlinear optical devices due to their significant nonlinear responses. Strong second-harmonic generation (SHG) from this group of materials has been reported with a large second-order optical nonlinearity significantly higher than the values observed for other 2D nonlinear materials.[13–21] Particularly, niobium oxide dichloride ($NbOCl_2$) has been used to build compact and efficient quantum light sources to generate the correlated photon pairs via the spontaneous parametric down-conversion process, based on its unique properties of weak interlayer electronic coupling and strong second-order optical nonlinearity.[14,17] The SHG from $NbOX_2$ crystals exhibits an anisotropic response that is dependent on the excitation wavelength and can be modified by applying strain or external pressure to the crystal.[13,16,19–21] The anisotropic optical response of 2D materials has gained significant research interest as a promising platform for building ultrathin polarization-sensitive optical devices.[22–26] Furthermore, $NbOX_2$ crystals can exhibit ferroelectric-to-paraelectric or

J. Deka, X. Yang
Department of Mechanical and Aerospace Engineering
Missouri University of Science and Technology
Rolla, MO 65409, USA
E-mail: yangxia@mst.edu
J. Gao
Department of Mechanical Engineering
Stony Brook University
Stony Brook, NY 11794, USA
E-mail: jie.gao.5@stonybrook.edu

The ORCID identification number(s) for the author(s) of this article can be found under https://doi.org/10.1002/lpor.202501523

DOI: 10.1002/lpor.202501523

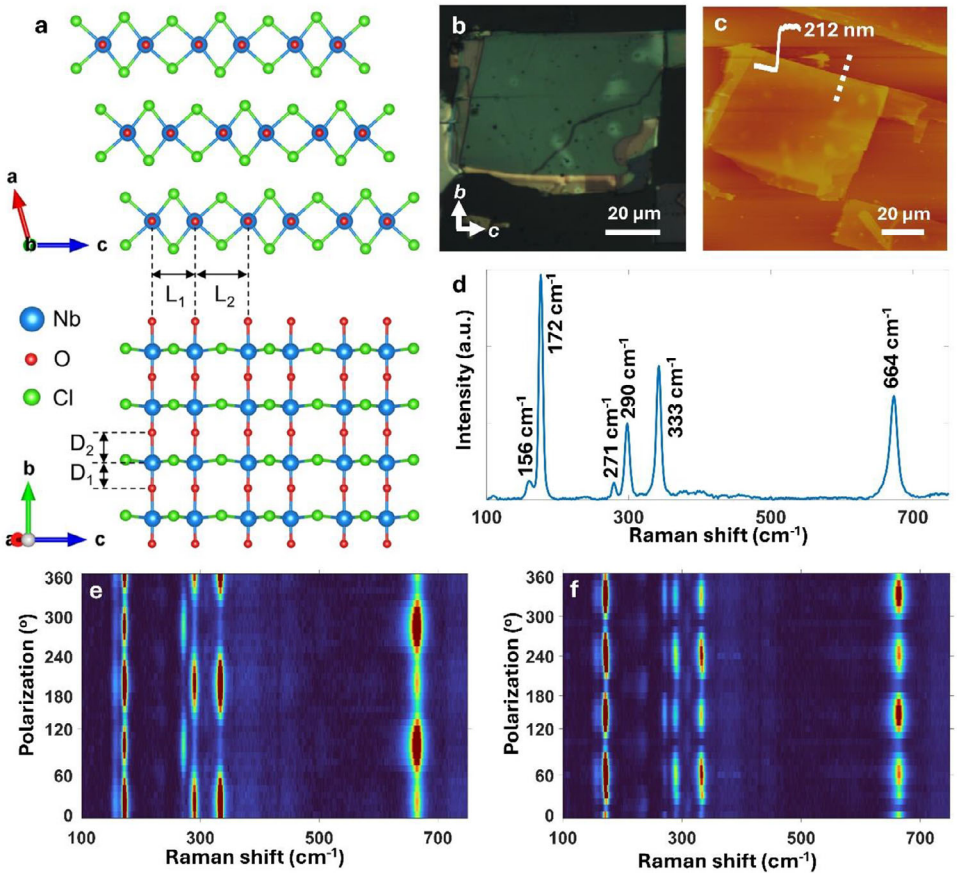

Figure 1. a) Side view and top view of the $NbOCl_2$ lattice structure. b) Optical microscope image, and (c) AFM image of the 212 nm-thick $NbOCl_2$ flake transferred on glass substrate. The line scan for measuring the flake thickness is shown in the inset of the AFM image. d) Raman spectrum of the flake with the A_g modes labeled. Contour plots of the polarization-resolved Raman spectra of the flake for e) parallel and f) perpendicular components.

ferroelectric-to-antiferroelectric (FE-to-AFE) phase transition under external stimuli such as temperature, strain, and pressure, which is associated with the crystal structural distortion from non-centrosymmetric to centrosymmetric arrangement resulting in a sharp drop in SHG intensity.[15,16] The tunability of the SHG emission from $NbOX_2$ crystals with external stimuli is crucial in implementing various functional nonlinear photonic devices for applications in optical sensing, optical computing, and optical switching.[27–29]

In this work, anisotropic second-harmonic optical vortex beams are produced from ultrathin ferroelectric $NbOCl_2$ fork grating holograms. The temperature tuning of the SHG intensity of the generated optical vortex beam is demonstrated with the SHG intensity vanishing beyond the Curie temperature for the FE-to-AFE phase transition in $NbOCl_2$ crystal. The $NbOCl_2$ crystal is characterized by the polarization-resolved Raman spectroscopy to reveal the anisotropic responses of different Raman modes. Furthermore, it is shown that the anisotropic and temperature-tunable second-harmonic vortex beams can be generated irrespective of the relative orientation of the fork grating holograms with respect to the $NbOCl_2$ crystallographic orientation. From the theoretical fits of the polarization-dependent SHG intensity, the relative magnitudes of the second-order nonlinear susceptibility elements of the $NbOCl_2$ crystal are extracted. Moreover, the Curie temperature for the FE-to-AFE phase transition in $NbOCl_2$ crystal is determined based on the measured temperature-dependent SHG intensities from the bare flakes and the fabricated holograms. These results unlock new possibilities for developing advanced multifunctional polarization-sensitive and temperature-tunable nonlinear photonic devices for future applications in integrated photonic devices, quantum optical chips, optical sensing, and optical communication.

2. Results and Discussion

The side view and top view of the $NbOCl_2$ lattice structure are illustrated in **Figure 1**a. The $NbOCl_2$ layers are stacked along the *a*-axis with weak van der Waals forces, with the interlayer distance of 0.65 nm.[14] The $NbOCl_2$ lattice has a monoclinic structure belonging to the C2 space group. The Nb atoms present a one-dimensional Peierls distortion, which results in the unequal distances between two Nb atoms along the *c*-axis ($L_1 \neq L_2$) and the unequal distances of an Nb atom from two neighboring O atoms along the *b*-axis ($D_1 \neq D_2$). The displacement of the Nb atoms causes the separation of charge centers, which leads to a spontaneous polarization along the *b*-axis. The generated spontaneous polarization will induce a strong second-order nonlinear susceptibility in the $NbOCl_2$ crystal, with the relatively stronger

nonlinear susceptibility element $\chi^{(2)}_{bbb}$ compared to the nonlinear susceptibility element $\chi^{(2)}_{bcc}$. The anisotropy of the second-order nonlinear susceptibility will result in the anisotropic SHG response from the $NbOCl_2$ crystal. Recently, the second-order nonlinear susceptibility elements in the $NbOCl_2$ crystal have been studied using density functional theory calculations,[16] which show that the nonlinear susceptibility elements $\chi^{(2)}_{bbb}$ and $\chi^{(2)}_{bcc}$ along the polar directions display noticeable values, while $\chi^{(2)}_{bbb}$ exhibits a relatively larger value than $\chi^{(2)}_{bcc}$ over a wide frequency range, demonstrating the distinctive role of ferroelectricity in driving the anisotropic SHG response in the $NbOCl_2$ crystal. First, polarization-resolved Raman spectroscopy is performed on the $NbOCl_2$ crystal to identify the crystallographic orientations. Figure 1b,c shows the optical microscope image and the atomic force microscopy (AFM) image of the exfoliated $NbOCl_2$ flake on a glass substrate. From the line scan of the AFM image, the flake thickness is determined to be ≈212 nm. The Raman spectrum of the flake excited with a 632.8 nm He-Ne laser is shown in Figure 1d, depicting six distinct Raman peaks for the A_g modes located at 156, 172, 271, 290, 333, and 664 cm^{-1}, together with two additional weak Raman peaks for the B_g modes at 234 and 310 cm^{-1}. The polarization-resolved Raman spectra for the parallel and perpendicular components are depicted as contour plots in Figure 1e,f. It is shown that the Raman mode intensities exhibit periodic variations as a function of the excitation polarization angle. To further resolve the anisotropic Raman modes, the polar plots of the parallel and perpendicular components of each Raman mode are plotted in **Figure 2**, with Figure 2a–f showing the A_g modes and Figure 2g,h showing the B_g modes. All Raman modes are observed to have highly anisotropic responses, with the Raman intensities showing either two-fold or four-fold patterns depending on the excitation polarization angle. For the A_g modes at 156, 172, 290, and 333 cm^{-1}, the Raman intensity maxima for the parallel components occur when the excitation polarization is along the *c*-axis of the $NbOCl_2$ crystal, with the secondary maxima occurring along the *b*-axis for the modes at 156 and 172 cm^{-1}. Whereas for the A_g modes at 271 and 664 cm^{-1}, the Raman intensity maxima for the parallel components are observed along the *b*-axis, with the secondary maximum occurring along the *c*-axis for the mode at 664 cm^{-1}. For all the A_g modes, the perpendicular components of the Raman intensities exhibit four-fold patterns with the intensity maxima occurring approximately along 45° and 135° with respect to the crystallographic *c*-axis. For the cases of the B_g modes, both parallel and perpendicular components display four-fold patterns, where the intensity maxima for the parallel components appear approximately along 45° and 135° to the *c*-axis, but the intensity maxima for the perpendicular components occur along both *b*-axis and *c*-axis. Next, the measured Raman intensity polar plots are correlated with the theoretical model. For $NbOCl_2$, belonging to the monoclinic crystal structure with C2 space group, the polarization-dependent Raman intensities of the parallel and perpendicular components for the A_g and B_g modes can be expressed as,

$$I_{\parallel}\left(A_g\right) \propto |a|^2 cos^4\theta + |b|^2 sin^4\theta + \frac{|a|\,|b|}{2} cos\phi_{ab} sin^2 2\theta \quad (1)$$

$$I_{\perp}\left(A_g\right) \propto \frac{1}{4}\left(|a|^2 + |b|^2 - 2\,|a|\,|b|\,cos\phi_{ab}\right) sin^2 2\theta \quad (2)$$

$$I_{\parallel}\left(B_g\right) \propto |f|^2 sin^2 2\theta \quad (3)$$

$$I_{\perp}\left(B_g\right) \propto |f|^2 cos^2 2\theta \quad (4)$$

where θ is the excitation polarization angle with respect to the *c*-axis of the crystal, *a*, *b*, and *f* are the complex amplitudes of Raman tensor elements, with ϕ_{ab} being the phase difference between *a* and *b*. The fitted Raman intensity polar plots (red solid lines) depicted in Figure 2 shows good agreement with the experimental data (black dots). According to the theoretical fits, the crystallographic *b* and *c* directions can be retrieved, which are also depicted in Figure 1b.

The crystallographic orientations of the $NbOCl_2$ crystal are further investigated with both the polarization-resolved Raman spectroscopy and SHG measurements. **Figure 3**a,b shows the optical microscope image and the AFM image of another exfoliated $NbOCl_2$ flake. From the line scan of the AFM image, the thickness of the flake is determined to be 22 nm. The parallel components of the Raman intensities for the A_g modes at 290 and 664 cm^{-1} are plotted in Figure 3c,d (black dots) along with the theoretical fits (red solid lines) using Equation (1). Consistent with the measurements presented in Figure 2 for the much thicker flake, it is shown that both the A_g modes at 290 and 664 cm^{-1} exhibit two-fold polarization-dependent profiles with the intensity maxima occurring along the crystallographic *c*-axis and *b*-axis, respectively. Next, SHG measurements are performed on the flake at the excitation wavelength of 900 nm. Figure 3e plots the SHG spectrum with a peak at 450 nm, which is exactly half of the excitation wavelength. To further confirm the SHG process, the pump power dependence of the nonlinear signal is plotted in Figure 3f in a log-log scale. The power law fit of the experimental data gives a slope of 2.01, which is consistent with the SHG process. The polarization-resolved SHG intensity for the 22 nm-thick flake is plotted in Figure 3g, which shows the highly anisotropic SHG response from the $NbOCl_2$ crystal with the maximum total SHG intensity occurring as the pump polarization is along the crystallographic *b*-axis. Both the parallel and perpendicular components of SHG intensity display two-fold polarization-dependent profiles with the intensity maxima appearing along the *b*-axis and *c*-axis, respectively. For the $NbOCl_2$ crystal belonging to a monoclinic crystal structure with the C2 space group, the parallel and perpendicular components of SHG intensity can be written as,

$$I^{\parallel}_{2\omega} \propto \left|3\chi^{(2)}_{bcc} cos^2\theta sin\theta + \chi^{(2)}_{bbb} sin^3\theta\right|^2 \quad (5)$$

$$I^{\perp}_{2\omega} \propto \left|\chi^{(2)}_{bcc} cos^3\theta - 2\chi^{(2)}_{bcc} sin^2\theta cos\theta + \chi^{(2)}_{bbb} sin^2\theta cos\theta\right|^2 \quad (6)$$

where θ is the polarization angle of the pump beam with respect to the *c*-axis of the crystal, $\chi^{(2)}_{bbb}$ and $\chi^{(2)}_{bcc}$ represent the two independent second-order nonlinear susceptibility elements. Figure 3g also plots the theoretical fits with solid lines, which agree with the measured data well. The parallel component of SHG emission is much stronger than the perpendicular component, resulting in the highly anisotropic two-fold profile for the total SHG intensity

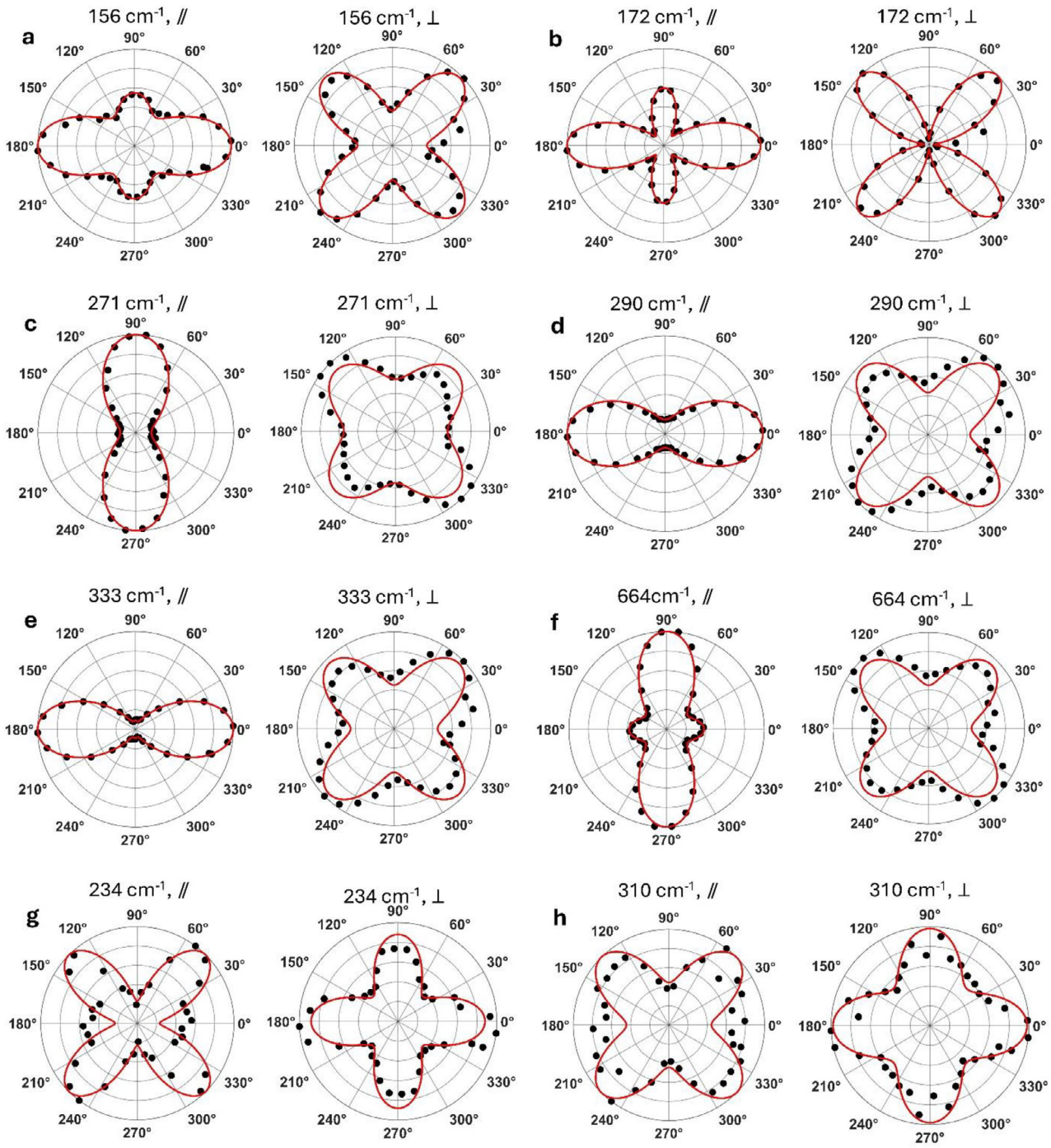

Figure 2. Polar plots of the Raman intensities of the parallel and perpendicular components for a–f) the A_g modes at 156, 172, 271, 290, 333, and 664 cm^{-1}, and g,h) the B_g modes at 234 and 310 cm^{-1} for the 212 nm-thick $NbOCl_2$ flake. The crystallographic *b*-axis is aligned with the vertical direction.

where the intensity maxima occur along the *b*-axis (polar axis) and the minima appear along the *c*-axis (non-polar axis).

The fork grating holograms are created to generate second-harmonic vortex beams by encoding the amplitude and phase information of the beam on the $NbOCl_2$ crystal. The binary amplitude modulation of the second-order nonlinear susceptibility of the $NbOCl_2$ crystal is considered as,

$$\chi^{(2)}(x,y) = \chi^{(2)}\left\{\frac{1}{2}+\frac{1}{2}sgn\left[cos\left\{\frac{2\pi x}{\Lambda}-\phi(x,y)\right\}-cos\left\{sin^{-1}A(x,y)\right\}\right]\right\} \quad (7)$$

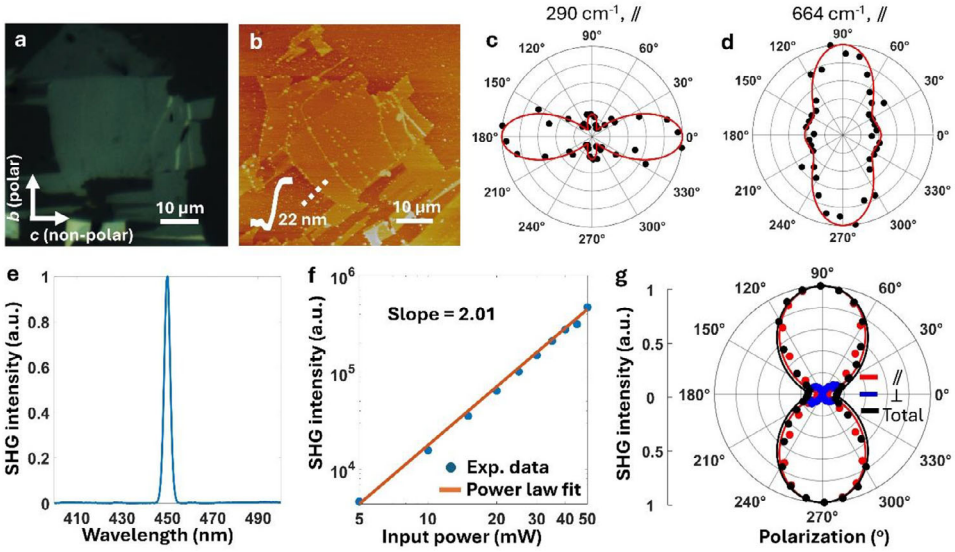

Figure 3. a) Optical microscope image and b) AFM image of the 22 nm-thick $NbOCl_2$ flake transferred on glass substrate. c,d) Parallel components of the Raman intensities for the A_g modes at 290 and 664 cm^{-1}. Black dots are the measured data and red solid lines represent the theoretical fits. e) SHG spectrum of the flake. f) Pump power dependence of the SHG signal in log-log plot. g) Parallel component, perpendicular component, and total SHG intensity depending on the pump polarization angle shown as red, blue and black dots, respectively. The theoretical fits are depicted as solid lines.

where Λ represents the grating period, $A(x, y)$ and $\phi(x, y)$ represent the amplitude and phase profiles of the beam wavefront in the hologram plane. With the amplitude profile of $A(x, y) = 1$, the required phase profile to generate a second-harmonic vortex beam with topological charge TC = l can be written as,

$$\phi\ (x, y) = \begin{cases} l \cdot tan^{-1}\,(y/x) & x \geq 0 \\ l \cdot \left[tan^{-1}\,(y/x) + \pi\right] & x < 0 \end{cases} \tag{8}$$

The second-harmonic vortex beams with TC = $\pm l$ will be produced in the first diffraction order at the diffraction angle calculated by $\theta_{SHG} = sin^{-1}(\lambda_{SHG}/\Lambda)$ with the second-harmonic wavelength λ_{SHG} and the grating period Λ. The fork grating holograms are fabricated by using focused ion beam (FIB) to directly mill patterns into the $NbOCl_2$ thin flakes, with the design parameters of the grating period Λ = 2.4 μm, the topological charge l = 1, and the FIB patterning area of 20 × 20 μm^2. **Figure** 4a,b shows the optical microscope image and the scanning electron microscopy (SEM) image of the fabricated fork grating hologram with the grating lines aligned with the crystallographic *b*-axis of the $NbOCl_2$ flake. Prior to the FIB patterning, the thickness of the flake is measured to be 85 nm using AFM, as shown by the line scan plot in the inset of Figure 4a. Figure 4c shows the second-harmonic image of the fork grating hologram when excited with the 900 nm pump beam. The corresponding far-field image of the hologram in the Fourier plane is shown in Figure 4d, demonstrating the generation of the second-harmonic vortex beams in the first diffraction order. The diffraction angle is determined as ≈10.8°. The TCs of the vortex beams are determined by using the astigmatic transformation of the far-field image with a cylindrical lens, as shown in Figure 4e. The TCs can be obtained from the number of dark stripes and the stripe orientation in the transformed image, which are determined as +1 and −1 for the vortex beams on the left and right sides of the central spot, respectively. Figure 4f plots the pump polarization angle dependence of the SHG intensity from the bare flake and the SHG intensity of the vortex beam. Highly anisotropic SHG responses are observed with a two-fold polarization-dependent profile, with the SHG intensity maxima occurring along the crystallographic *b*-axis of the $NbOCl_2$ flake. The measured anisotropy ratios representing the ratio of the maximum and minimum SHG intensities are 5.88 and 6.59 for the bare flake and the vortex beam, respectively. The variations in the anisotropy ratios between the bare flake and the vortex beam can be attributed to the contamination of the crystal during the FIB milling process, which can alter the crystal structure. Furthermore, the temperature dependence of the SHG intensity is plotted separately for the bare flake and the vortex beam in Figure 4g. It is observed that the SHG intensity gradually decreases with the increase in temperature and becomes negligible as the temperature approaches the Curie temperature when the $NbOCl_2$ crystal transitions from FE to AFE phase. The images of second-harmonic vortex beams at the temperatures of 303, 333, and 363 K are displayed in the inset of Figure 4g, which demonstrates the temperature-tunable SHG intensity of the generated vortex beam. The temperature dependence of the SHG intensity near the Curie temperature of a ferroelectric material can be described as,

$$I_{SHG} \propto \left|\chi^{(2)}\right|^2 \propto P_s^2 \propto \left(T_c - T\right) \tag{9}$$

where P_s is the spontaneous polarization and T_c is the Curie temperature.[30,31] Figure 4g also plots the theoretical fits (solid lines) for the measured temperature-dependent SHG intensity, showing a good agreement with the measured data. It is shown that the SHG intensity decreases almost linearly with temperature due to the weakening of spontaneous polarization as the temperature increases. At room temperature, the $NbOCl_2$ crystal

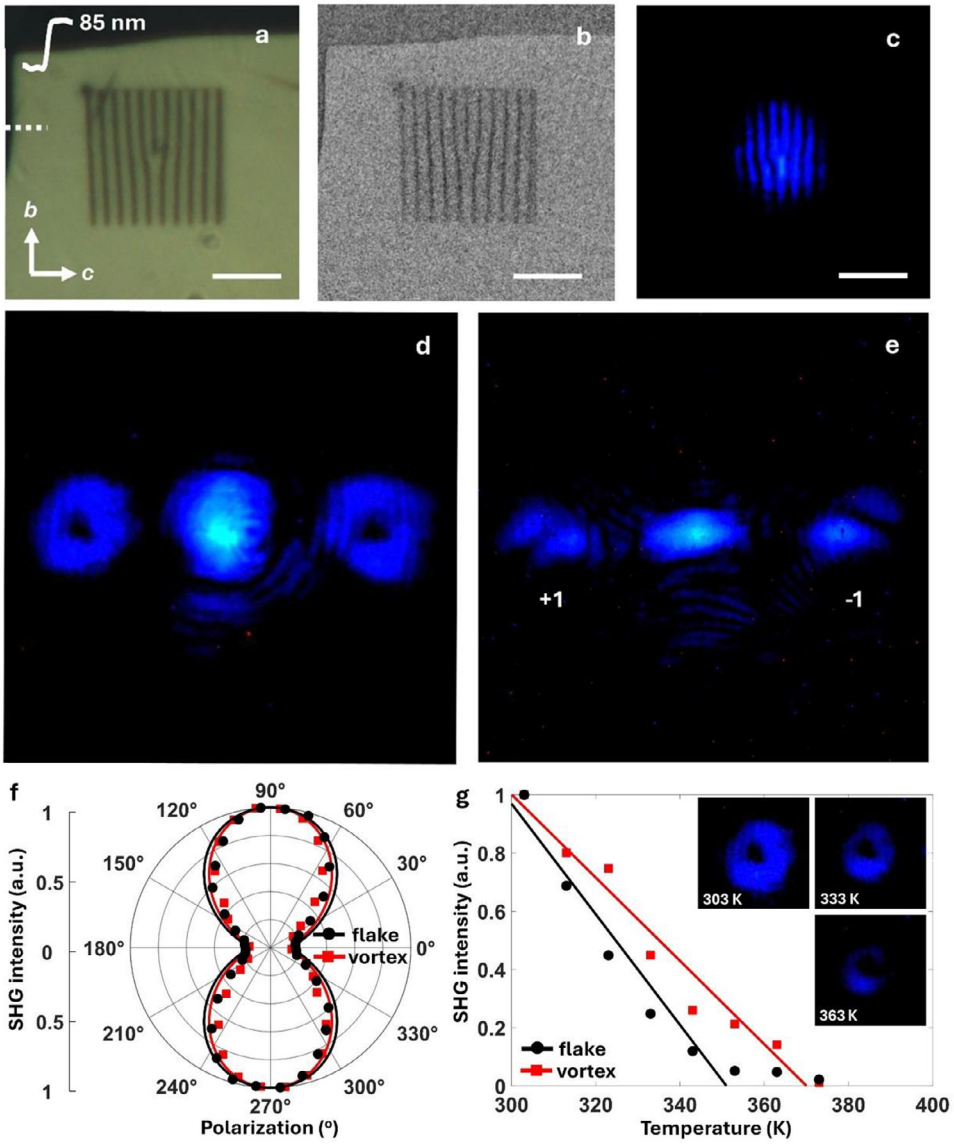

Figure 4. Second-harmonic vortex beam generation with the fork grating hologram oriented at 0° to the *b*-axis. a) Optical microscope image, b) SEM image and c) second-harmonic image of the hologram. All scale bars are 10 μm. d) Far-field image of the hologram with the generated vortex beams. e) Cylindrical lens transformed image with the topological charges marked. f) Polarization angle dependence of the SHG intensity for the bare flake (black dots) and the vortex beam (red squares). The theoretical fits are depicted as solid lines. The crystallographic *b*-axis is in the vertical direction. g) Temperature dependence of the SHG intensity for the bare flake (black dots) and the vortex beam (red squares). Solid lines are the linear fits to the experimental data. The second-harmonic vortex images at temperatures approaching the Curie temperature are shown in the inset.

exhibits the FE phase with a non-centrosymmetric C2 structure, giving the strong SHG intensity. As the temperature increases, the AFE phase begins to mix with the FE phase and gradually takes dominance over the FE phase, which leads to the continuous reduction of the SHG intensity. As the temperature reaches the Curie temperature, the FE phase is fully converted into the AFE phase with a centrosymmetric C2/c structure, resulting in the vanishing SHG intensity. From the theoretical fits, the retrieved values of the Curie temperature for the bare flake and the fabricated hologram are 351 and 370 K, respectively. The variations of the T_c values between the bare flake and the hologram can be attributed to the defects introduced in the $NbOCl_2$ crystal during the FIB milling process with gallium ions.

Next, the second-harmonic vortex beam generation is investigated by rotating the relative orientation of the fork grating hologram with respect to the crystallographic orientation of the $NbOCl_2$ flake. The optical microscope image, SEM image, and second-harmonic image of the fabricated fork grating hologram oriented approximately along 45° to the crystallographic *b*-axis are shown in **Figure** 5a–c. The flake thickness is determined to be 63 nm from the line scan obtained from the AFM image, as depicted in the inset of Figure 5a. The far-field image of the holo-

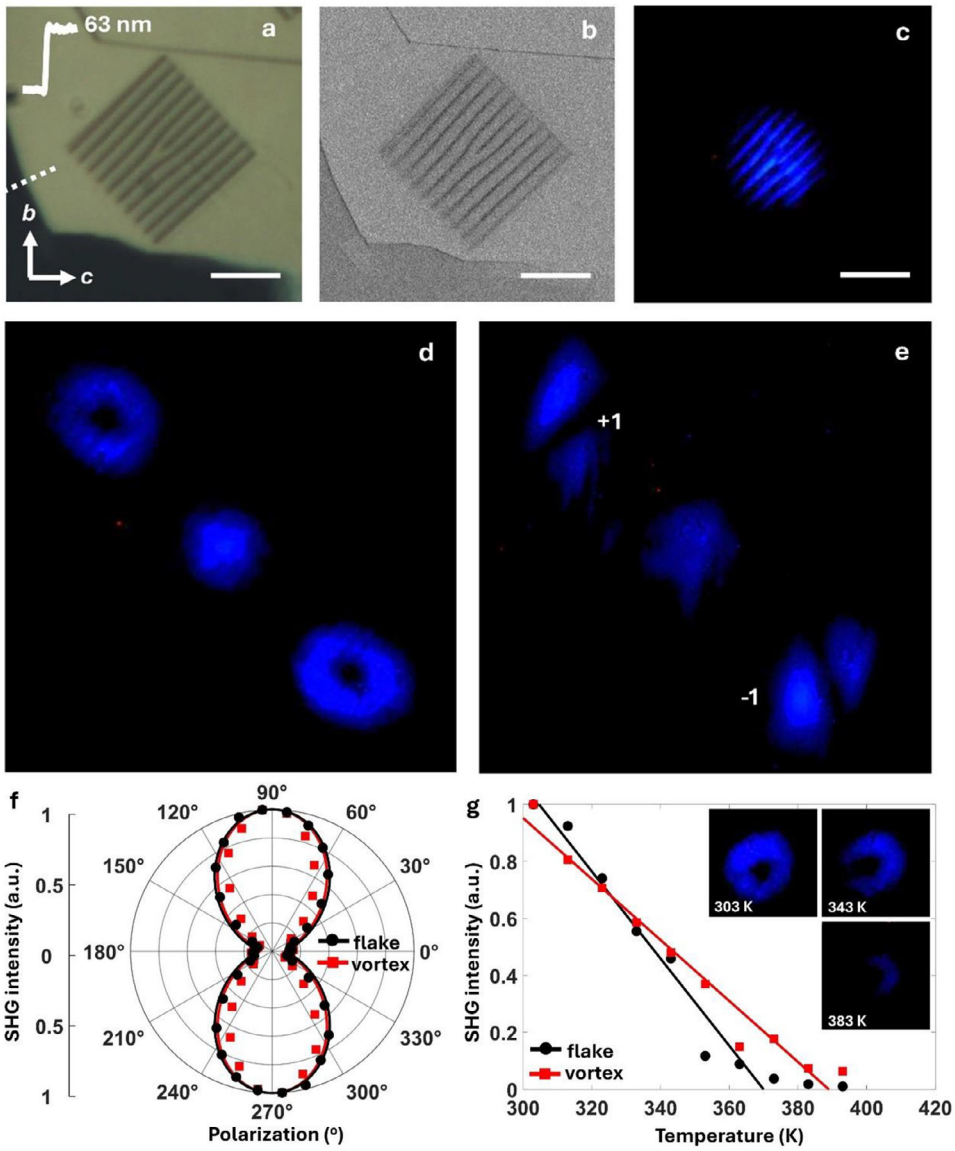

Figure 5. Second-harmonic vortex beam generation with the fork grating hologram oriented at 45° to the *b*-axis. a) Optical microscope image, b) SEM image and c) second-harmonic image of the hologram. All scale bars are 10 μm. d) Far-field image of the hologram. e) Cylindrical lens transformed image with the topological charges marked. f) Polarization angle dependence of the SHG intensity for the bare flake (black dots) and the vortex beam (red squares). The theoretical fits are depicted as solid lines. g) Temperature dependence of the SHG intensity for the bare flake (black dots) and the vortex beam (red squares). Solid lines are the linear fits to the experimental data. The second-harmonic vortex images at temperatures approaching the Curie temperature are shown in the inset.

gram shown in Figure 5d demonstrates the production of the second-harmonic vortex beams. The cylindrical lens transformed image shown in Figure 5e indicates the TCs of +1 and −1 for the vortex beams on the upper left and lower right corners, respectively. The polarization-dependent SHG intensity from the bare flake and the SHG intensity of the vortex beam are plotted in Figure 5f, showing two-fold profiles with the intensity maxima occurring along the *b*-axis. The theoretical fits to the experimental data using Equations (5) and (6) are also plotted as solid lines. The measured anisotropy ratios for the bare flake and the vortex beam are determined to be 9.37 and 10.17, respectively. The temperature-dependent SHG intensity for the bare flake and the vortex beam plotted in Figure 5g demonstrates that the SHG intensity is reduced as the temperature increases, and it becomes negligible at temperatures approaching the Curie temperature of the $NbOCl_2$ crystal. According to the theoretical fits using Equation (9) shown as solid lines, the Curie temperatures for the bare flake and the fabricated hologram are 370 and 389 K, respectively. The second-harmonic vortex images at the temperatures of 303, 343, and 383 K displayed in the inset of Figure 5g further demonstrate the temperature tunability of the vortex beam intensity. The measurements are further conducted for the fork grating hologram oriented along 90° to the crystallographic *b*-axis, which is along the *c*-axis, with the optical microscope image, SEM

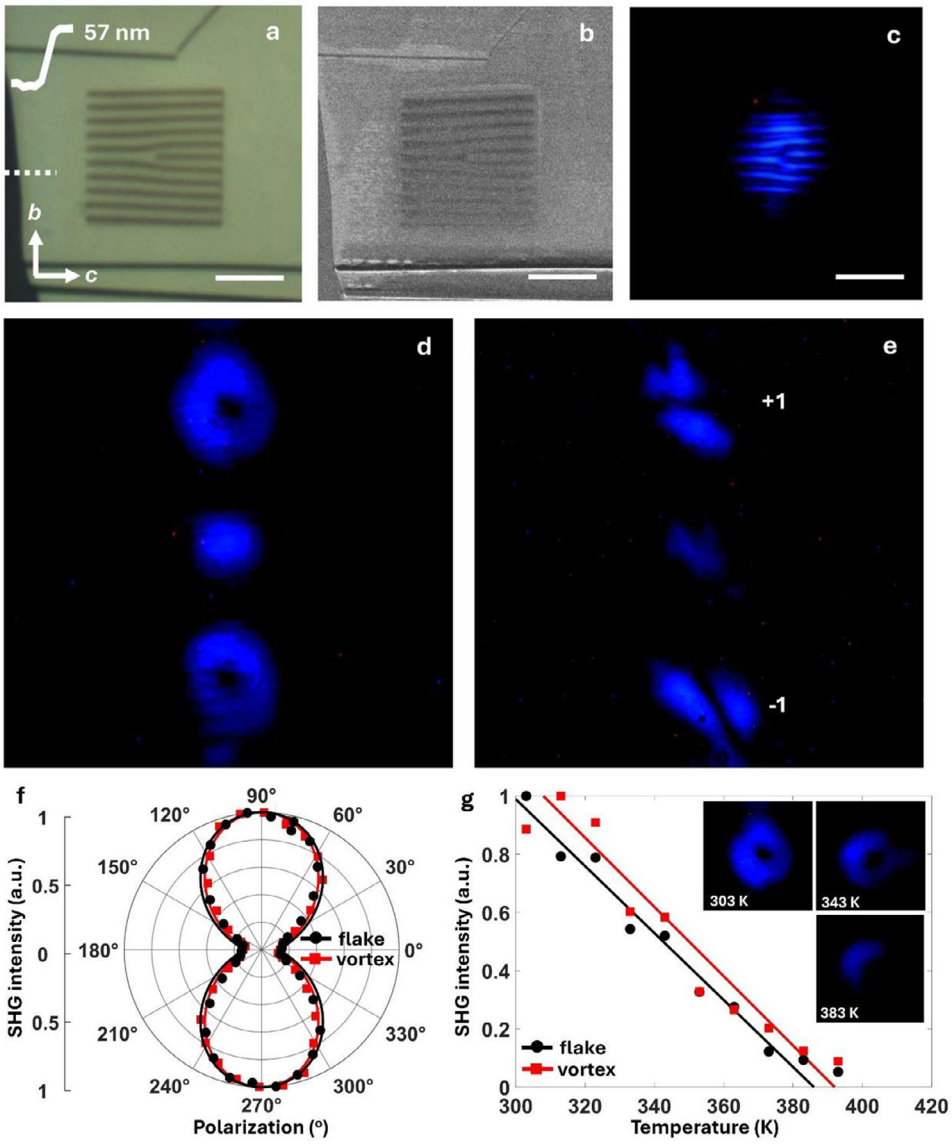

Figure 6. Second-harmonic vortex beam generation with the fork grating hologram oriented at 90° to the *b*-axis. a) Optical microscope image, b) SEM image and c) second-harmonic image of the hologram. All scale bars are 10 μm. d) Far-field image of the hologram. e) Cylindrical lens transformed image with the topological charges marked. f) Polarization angle dependence of the SHG intensity for the bare flake (black dots) and the vortex beam (red squares). The theoretical fits are depicted as solid lines. g) Temperature dependence of the SHG intensity for the bare flake (black dots) and the vortex beam (red squares). Solid lines are the linear fits to the experimental data. The second-harmonic vortex images at temperatures approaching the Curie temperature are shown in the inset.

image, and second-harmonic image shown in **Figure 6**a–c. The flake thickness is measured as 57 nm according to the line scan of the AFM image shown in the inset of Figure 6a. The corresponding far-field image of the hologram and the cylindrical lens transformed image in Figure 6d,e demonstrate the generation of the vortex beams in the first diffraction order on the upper and lower sides of the central spot with the TCs of +1 and −1, respectively. The polarization-dependent SHG intensity for the bare flake and the vortex beam are plotted in Figure 6f along with the theoretical fits. Like the cases of the fork grating holograms oriented along 0° and 45° to the *b*-axis, the fork hologram oriented along the *c*-axis is also found to have a highly anisotropic response. The anisotropy ratios for the bare flake and the vortex beam are 7.21 and 8.27, respectively. Figure 6g plots the temperature-dependent SHG intensity for the bare flake and the vortex beam along with the theoretical fits, showing the Curie temperatures for the bare flake and the fabricated hologram as 386 and 392 K, respectively. The second-harmonic vortex images presented in the inset of Figure 6g at the increased temperatures show a gradual reduction of the vortex beam intensity as the temperature approaches the Curie temperature.

The SHG conversion efficiency of the hologram, $\eta_{CE,}$ is calculated by the ratio between the total SHG power and the pump power. For the 0° and 90° oriented fork grating holograms, the

Table 1. List of the relative magnitudes of second-order nonlinear susceptibility elements of $NbOCl_2$ crystal, the theoretical and measured SHG anisotropy ratios, and the Curie temperatures for the bare flakes and the fabricated holograms.

Sample	$\chi^{(2)}_{bbb}$	$\chi^{(2)}_{bcc}$	$\lvert\chi^{(2)}_{bbb}/\chi^{(2)}_{bcc}\rvert^2$	SHG ratio	T_c
0° flake/vortex	1	0.41/0.37	5.95/7.30	5.88/6.59	351 K/370 K
45° flake/vortex	1	0.33/0.30	9.18/11.11	9.37/10.17	370 K/389 K
90° flake/vortex	1	0.38/0.34	6.92/8.65	7.21/8.27	386 K/392 K

average pump power is 40 mW and the peak irradiance is 2.48 GW cm^{-2}, while for the 45° oriented hologram, the average pump power is 32 mW with the peak irradiance of 1.98 GW cm^{-2}. The SHG conversion efficiencies are determined to be 1.88×10^{-10}, 2.25×10^{-10}, and 8.75×10^{-11} for the 0°, 45° and 90° oriented holograms, respectively. The second-harmonic vortex conversion efficiency for the generated vortex beam is determined by $\eta_{\text{vortex}} = \eta_{\text{CE}} \cdot \eta_{\text{DE}}$, where η_{DE} is the diffraction efficiency of the vortex beam in the first diffraction order. The diffraction efficiencies are calculated to be 42.8%, 76.4%, and 79.5% for the 0°, 45°, and 90° oriented holograms, respectively. The diffraction efficiency of the 0° oriented hologram is found to be significantly lower than the other two holograms, which may be associated with the quality of hologram fabrication during the FIB milling process. Finally, the second-harmonic vortex conversion efficiencies are calculated as 8.05×10^{-11}, 1.72×10^{-10}, and 6.96×10^{-11} for the 0°, 45°, and 90° oriented holograms, respectively.

The relative magnitudes of the second-order nonlinear susceptibility elements of the $NbOCl_2$ crystal can be extracted from the theoretical fits of the measured polarization-dependent SHG intensity by using Equations (5) and (6), which are listed in **Table 1**. The relative magnitudes of $\chi^{(2)}_{bcc}$ are found to be in the range from 0.30 to 0.41 for the bare flakes and the fabricated holograms. The theoretical SHG anisotropy ratio can be calculated from the square of the ratio $\chi^{(2)}_{bbb}/\chi^{(2)}_{bcc}$ which is also listed in Table 1 along with the measured SHG anisotropy ratio. The theoretical SHG anisotropic ratios varying from 5.95 to 11.11 are consistent with the measured ones from 5.88 to 10.17. The variations in the SHG anisotropy ratios between different bare flakes can be associated with different levels of strain introduced to the crystal during the mechanical exfoliation process, which have been observed in other 2D materials.[32,33] Meanwhile, the variations between the bare flakes and the fabricated holograms can be explained by the defects introduced during the FIB milling process, which can alter the $NbOCl_2$ crystal structure. The Curie temperatures T_c for the FE-to-AFE phase transition in $NbOCl_2$ crystal are also listed in Table 1. The T_c values are in the range from 351 to 392 K for different bare flakes and fabricated holograms considered here. The variations of T_c between the bare flakes can be attributed to the strain effects from the mechanical exfoliation process or the flake thickness-related size effects,[15,34] while the variations of T_c between the bare flakes and the fabricated holograms can be related to the defects introduced into the crystal during the FIB milling process with gallium ions. It is noteworthy that the gallium ion contamination can alter the lattice structure and electronic properties of the $NbOCl_2$ crystal, leading to the modifications of the second-order nonlinear susceptibility elements, thus the SHG anisotropy ratio and the Curie temperature for the fabricated hologram are changed compared to the bare flake.

3. Conclusion

In summary, we have demonstrated highly anisotropic and temperature-tunable second-harmonic vortex beam generation from ultrathin ferroelectric $NbOCl_2$ fork grating holograms. The $NbOCl_2$ crystal is characterized by polarization-resolved Raman spectroscopy, which shows the anisotropic responses of the Raman modes. The polarization-resolved SHG measurements are performed to show the highly anisotropic SHG response from the $NbOCl_2$ crystal, with the maximum intensity occurring along the crystallographic *b*-axis. It is demonstrated that the anisotropic and temperature-tunable second-harmonic vortex beams can be produced independently of the relative orientation of the fork grating hologram with respect to the $NbOCl_2$ crystallographic orientation. High anisotropy ratios for the vortex beams reaching up to 10.17 are achieved, with the maximum SHG intensity of the vortex beam occurring along the *b*-axis. The temperature tunability of the SHG intensity of the vortex beam is demonstrated, with the intensity becoming negligible as the temperature approaches the Curie temperature for the FE-to-AFE phase transition in the $NbOCl_2$ crystal. Furthermore, the relative magnitudes of the second-order nonlinear susceptibility elements and the Curie temperature of the $NbOCl_2$ crystal are extracted using the theoretical fits to the measured SHG intensities from the bare flakes and the fabricated holograms. Our demonstrated results enable new potential for advancing multifunctional polarization-responsive and temperature-switchable nonlinear optical devices used for future applications in integrated photonic devices, quantum optical chips, optical sensing, and optical communication. One promising application is integrating the ultrathin $NbOCl_2$ fork grating holograms onto the facets of waveguides or optical fibers to realize compact OAM multiplexers and demultiplexers for next-generation high-capacity optical communication systems.[35]

4. Experimental Section

Sample Preparation: $NbOCl_2$ thin flakes are obtained by mechanical exfoliation from bulk crystals (HQ graphene) in multiple times with scotch tape first and then Nitto tape (SPV 224). The flakes are then transferred to polydimethylsiloxane films and inspected with optical microscope to confirm the quality, size, and thickness of the flakes. Subsequently, the flakes are trans-

ferred to glass substrates using the dry transfer technique. The glass substrates are cleaned before the flake transfer using acetone and isopropyl alcohol. A water-soluble conductive polymer layer is spin-coated on the sample for surface charge dissipation during the subsequent FIB patterning step. The fork holograms are fabricated using FIB milling of the $NbOCl_2$ flakes with gallium ions to create the patterned area of $20 \times 20\ \mu m^2$ (FEI Helios Nanolab 600, accelerating voltage 30 kV, beam current 1.5 pA). The gallium ion contamination of the crystal during FIB milling is minimized by carefully optimizing the ion dose, dwell time, and beam astigmatism. The conductive polymer layer is subsequently removed by rinsing the sample with deionized water, and the sample is blown dry with nitrogen gas.

Optical Setup: For polarization-resolved Raman spectroscopy measurements, a 632.8 nm He-Ne laser beam is transmitted through a linear polarizer and a half-wave plate and focused on the sample with a 60× objective lens (NA = 0.85). The back-reflected signal is passed through a 633 nm ultrasteep long-pass edge filter (Semrock, LP02-633RE-25) and measured using an optical spectrometer (Horiba, iHR550). A linear polarization analyzer is used in the detection path to resolve the parallel and perpendicular components of the Raman spectrum. For the SHG measurements, the pump laser beam at 900 nm from a Ti:Sapphire oscillator (Coherent Chameleon, repetition rate 80 MHz, pulse width <100 fs) is transmitted through a linear polarizer and a half-wave plate and focused on the sample using a 4× objective lens (NA = 0.12). The sample is mounted on a temperature-controlled stage (Linkam, THMS600), and the laser spot diameter is ≈16 µm to illuminate the hologram area. The transmitted signal from the sample is collected using a 20× objective lens (NA = 0.42) and passed through a 675 nm short-pass filter and a 450 nm bandpass filter to selectively detect the SHG emission. The SHG signal is imaged either in real space or Fourier space using a color charge-coupled device camera. A cylindrical lens is used for the astigmatic transformation of the far-field image to determine the topological charge of the optical vortex.

Acknowledgements

The authors acknowledge the support from the National Science Foundation under Grant Nos. ECCS-2226875, ECCS-2226948, DMR-2412218 and DMR-2412219. The authors thank the facility support from the Materials Research Center at Missouri S&T.

Conflict of Interest

The authors declare no conflict of interest.

Data Availability Statement

The data that support the findings of this study are available from the corresponding author upon reasonable request.

Keywords

2D materials, ferroelectricity, nonlinear optics, optical anisotropy, vortex beam

Received: June 17, 2025
Revised: August 19, 2025
Published online:

[1] Z. Wang, N. Zhang, X.-C. Yuan, *Opt. Express* **2011**, *19*, 482.
[2] H. Wu, Q. Zeng, X. Wang, C. Li, Z. Huang, Z. Xie, Y. He, J. Liu, H. Ye, Y. Chen, Y. Li, D. Fan, S. Chen, *Nanophotonics* **2023**, *12*, 1129.
[3] J. Ng, Z. Lin, C. T. Chan, *Phys. Rev. Lett.* **2010**, *104*, 103601.
[4] M. Gecevičius, R. Drevinskas, M. Beresna, P. G. Kazansky, *Appl. Phys. Lett.* **2014**, *104*, 231110.
[5] A. Mair, A. Vaziri, G. Weihs, A. Zeilinger, *Nature* **2001**, *412*, 313.
[6] M. P. J. Lavery, F. C. Speirits, S. M. Barnett, M. J. Padgett, *Science* **2013**, *341*, 537.
[7] F. Yue, D. Wen, J. Xin, B. D. Gerardot, J. Li, X. Chen, *ACS Photonics* **2016**, *3*, 1558.
[8] S. Chen, Y. Cai, G. Li, S. Zhang, K. W. Cheah, *Laser Photonics Rev.* **2016**, *10*, 322.
[9] Y. Bai, J. Yan, H. Lv, Y. Yang, *J. Opt.* **2022**, *24*, 084004.
[10] J. W. You, S. R. Bongu, Q. Bao, N. C. Panoiu, *Nanophotonics* **2019**, *8*, 63.
[11] Z. Xie, T. Zhao, X. Yu, J. Wang, *Small* **2024**, *20*, 2311621.
[12] C. Trovatello, A. Marini, M. Cotrufo, A. Alù, P. J. Schuck, G. Cerullo, *ACS Photonics* **2024**, *11*, 2860.
[13] I. Abdelwahab, B. Tilmann, Y. Wu, D. Giovanni, I. Verzhbitskiy, M. Zhu, R. Berté, F. Xuan, L. d. S. Menezes, G. Eda, T. C. Sum, S. Y. Quek, S. A. Maier, K. P. Loh, *Nat. Photonics* **2022**, *16*, 644.
[14] Q. Guo, X. Qi, L. Zhang, M. Gao, S. Hu, W. Zhou, W. Zang, X. Zhao, J. Wang, B. Yan, M. Xu, Y. Wu, G. Eda, Z. Xiao, S. A. Yang, H. Gou, Y. P. Feng, G. Guo, W. Zhou, X. Ren, C. Qiu, S. J. Pennycook, A. T. S. Wee, *Nature* **2023**, *613*, 53.
[15] M. Huang, W. Chen, S. Luo, Z. Huang, Z. Wang, X. Qi, *Appl. Phys. Lett.* **2024**, *124*, 111901.
[16] L. Ye, W. Zhou, D. Huang, X. Jiang, Q. Guo, X. Cao, S. Yan, X. Wang, D. Jia, D. Jiang, Y. Wang, X. Wu, X. Zhang, Y. Li, H. Lei, H. Gou, B. Huang, *Nat. Commun.* **2023**, *14*, 5911.
[17] I. Abdelwahab, B. Tilmann, X. Zhao, I. Verzhbitskiy, R. Berté, G. Eda, W. L. Wilson, G. Grinblat, L. de S Menezes, K. P. Loh, S. A. Maier, *Adv. Optical Mater.* **2023**, *11*, 2202833.
[18] W. Chen, S. Zhu, R. Duan, C. Wang, F. Wang, Y. Wu, M. Dai, J. Cui, S. H. Chae, Z. Li, X. Ma, Q. Wang, Z. Liu, Q. J. Wang, *Adv. Mater.* **2024**, *36*, 2400858.
[19] H. Wang, Q. Chen, Y. Cao, W. Sang, F. Tan, H. Li, T. Wang, Y. Gan, D. Xiang, T. Liu, *Nano Lett.* **2024**, *24*, 3413.
[20] T. Fu, K. Bu, X. Sun, D. Wang, X. Feng, S. Guo, Z. Sun, Y. Fang, Q. Hu, Y. Ding, T. Zhai, F. Huang, X. Lü, *J. Am. Chem. Soc.* **2023**, *145*, 16828.
[21] Y. Ding, L. Yan, Y. Wu, L. Zhou, *J. Phys. Chem. Lett.* **2024**, *15*, 7191.
[22] X. Li, H. Liu, C. Ke, W. Tang, M. Liu, F. Huang, Y. Wu, Z. Wu, J. Kang, *Laser Photonics Rev.* **2021**, *15*, 2100322.
[23] S. H. Suk, S. B. Seo, Y. S. Cho, J. Wang, S. Sim, *Nanophotonics* **2024**, *13*, 107.
[24] H. Liu, Z. Li, Y. Yu, J. Lin, S. Liu, F. Pang, T. Wang, *Nanophotonics* **2020**, *9*, 1651.
[25] J. Wang, C. Z. Jiang, W. Q. Li, X. H. Xiao, *Adv. Optical Mater.* **2022**, *10*, 2102436.
[26] Y. Zhang, J. Wu, L. Jia, D. Jin, B. Jia, X. Hu, D. Moss, Q. Gong, *npj Nanophoton* **2024**, *1*, 28.
[27] F. Liu, L. You, K. L. Seyler, X. Li, P. Yu, J. Lin, X. Wang, J. Zhou, H. Wang, H. He, S. T. Pantelides, W. Zhou, P. Sharma, X. Xu, P. M. Ajayan, J. Wang, Z. Liu, *Nat. Commun.* *7*, 12357.
[28] J. Fu, N. Yang, Y. Liu, Q. Liu, J. Du, Y. Fang, J. Wang, B. Gao, C. Xu, D. Zhang, A. J. Meixner, G. Gou, F. Huang, L. Zhen, Y. Li, *Adv. Funct. Mater.* **2024**, *34*, 2308207.

[29] Y. Zhao, J. Zhao, Y. Guo, J. Zhao, J. Feng, Y. Geng, J. Yang, H. Gao, M. Yuan, L. Jiang, Y. Wu, *SmartMat.* **2022**, *3*, 657.
[30] R. Fei, W. Kang, L. Yang, *Phys. Rev. Lett.* **2016**, *117*, 097601.
[31] R. Xu, J. Huang, E. S. Barnard, S. S. Hong, P. Singh, E. K. Wong, T. Jansen, V. Harbola, J. Xiao, B. Y. Wang, S. Crossley, D. Lu, S. Liu, H. Y. Hwang, *Nat. Commun.* **2020**, *11*, 3141.
[32] A. Dasgupta, J. Gao, X. Yang, *Laser Photonics Rev.* **2020**, *14*, 1900416.
[33] H. Sar, J. Gao, X. Yang, *Sci. Rep.* **2020**, *10*, 14282.
[34] X. Y. Lang, Q. Jiang, *J. Nanopart. Res.* **2007**, *9*, 595.
[35] Z. Xie, S. Gao, T. Lei, S. Feng, Y. Zhang, F. Li, J. Zhang, Z. Li, X. Yuan, *Photonics Res.* **2018**, *6*, 743.